Acta Oceanol. Sin., 2023, Vol. 42, No. 6, P. 100–111
https://doi.org/10.1007/s13131-022-2144-8
http://www.aosocean.com
E-mail: ocean2@hyxb.org.cn

A new model for Doppler shift of C-band echoes backscattered from sea surface

Jianbo Cui[1], Yunhua Wang[1, 2*], Yanmin Zhang[1*], Huimin Li[3], Wenzheng Jiang[4], Yushi Zhang[5], Xin Li[5]

[1] College of Information Science and Engineering, Ocean University of China, Qingdao 266100, China

[2] Qingdao National Laboratory for Marine Science and Technology, Qingdao 266237, China

[3] School of Marine Sciences, Nanjing University of Information Science and Technology, Nanjing 210044, China

[4] First Institute of Oceanography, Ministry of Natural Resources, Qingdao 266061, China

[5] National Key Laboratory of Electromagnetic Environment/China Research Institute of Radiowave Propagation, Qingdao 266107, China

Received 11 April 2022; accepted 27 December 2022

Abstract

Within the framework of the two-scale scattering model, the Doppler shift of C-band radar return signals from the nonlinear sea surface are numerically evaluated. As an analytical approximation method, the Bragg resonance scattering method cannot accurately describe the backscattering field from sea surface. Therefore, in the two-scale scattering model, more accurate scattering coefficient (the normalized radar cross section, NRCS) evaluated by the C-band dual-polarized (HH/VV) empirical geophysical model function (CSAR model) is employed to replace the traditional Bragg NRCS to weight the Doppler shift. The numerical results indicate that there are obvious differences between the Doppler shift weighted by the CSAR NRCS and that weighted by the traditional Bragg NRCS. The hydrodynamic modulation of the large-scale waves is one of the important factors that affect the difference between the Doppler shift predicted in upwind and downwind directions. If the relaxation rate in the hydrodynamic modulation is set to be the angular frequency of the dominant water waves, the Doppler shift predicted by the numerical method can fit the results of the empirical model (C-band empirical geophysical model function, CDOP) well at moderate wind speed. Under low wind condition, the comparison shows that the empirical CDOP model appears to overestimate the Doppler shift. In order to facilitate the application, at the end of this paper a semi-empirical CSAR-DOP model, which is a polynomial fitting formula, is developed for evaluating the Doppler shift of C-band signals from time varying sea surface.

Key words: Doppler shift, microwave scattering, numerical simulation

Citation: Cui Jianbo, Wang Yunhua, Zhang Yanmin, Li Huimin, Jiang Wenzheng, Zhang Yushi, Li Xin. 2023. A new model for Doppler shift of C-band echoes backscattered from sea surface. Acta Oceanologica Sinica, 42(6): 100–111, doi: 10.1007/s13131-022-2144-8

1 Introduction

As the scattering elements on sea surface are moving under the actions of wind, waves and current, the frequency of a radar signal backscattered from oceanic surface thus experiences a Doppler shift, which is proportional to the line-of-sight velocity of the scattering facets and weighted by their backscattered power (Keller et al., 1986). Consequently, the Doppler features could provide information on the ocean dynamic conditions, in complement to the normalized radar cross section (NRCS) which is related to the surface roughness. Thus, the studies on Doppler features are of practical importance in a number of research areas such as sea surface wind retrieving, sea waves monitoring and oceanic surface current measuring (Chapron et al., 2005; Johannessen et al., 2005; Kudryavtsev et al., 2005; Karaev et al., 2008; Johnson et al., 2009). In recent years, the properties of Doppler spectrum from sea surface have been the subject of extensive investigations, both theoretically and experimentally (Crombie, 1955; Bass et al., 1968; Wright and Keller, 1971; Barrick, 1977; Lipa, 1978; Mouche et al., 2008).

On the theoretical side, Crombie (1955) first investigated the properties of Doppler spectrum based on Bragg theory in the early stage. In Barrick (1977), Barrick built a perturbative model based on a representation of sea waves up to second order, which has been widely used for HF and VHF radars. For microwaves, besides the Bragg theory, the Kirchhoff approximation (KA) and the small slope approximation (SSA) can also be used to predict the Doppler shift of the signals from sea surface (Mouche et al., 2008). However, it should be pointed out that the Doppler shift predicted by the Kirchhoff approximation method (KA), the Bragg theory, and the first-order small slope approximation (SSA-1) in co-polarized configuration are insensitive to the polarization state. And experiment results show that the Doppler shift of horizontally polarized signals are generally larger than those vertically polarized case. Bass et al. (1968) and Wright and Keller (1971) established a two-scale surface scattering model (TSM) which includes modulation by the large scale waves, and makes the results closer to the real sea surface situation. What's more, the polarization dependence of the Doppler shift can also be well explained by using the two scale surface scattering model. In Wang and Zhang (2011) and Wang et al. (2012, 2013), the differ-

Foundation item: The National Natural Science Foundation of China under contract No. 41976167; the Key Research and Development Program of Shandong Province (International Science and Technology Cooperation) under contract No. 2019GHZ023.
*Corresponding author, E-mail: yunhuawang@ouc.edu.cn; yanminzhang@ouc.edu.cn

ences between co-polarized have been explained by the TSM, and the effects of tilt and hydrodynamic modulation have also been analyzed, which gives a quantitative interpretation of Doppler shift of sea surface echo. Up to now, the two-scale surface model is still as the most practical model to theoretically describe the Doppler spectrum of microwave scattering from sea surface (Zavorotny and Voronovich, 1998; Fuks and Voronovich, 2002). In several researches (Zavorotny and Voronovich, 1998; Fuks and Voronovich, 2002; Wang and Zhang, 2011 ; Wang et al., 2012, 2013), however, it should be pointed out that the local NRCS is calculated by the Bragg scattering theory. As we all know, the scattering coefficient calculated by the Bragg scattering theory generally has an obvious discrepancy with the actual signal backscattered from sea surface in real condition. Compared with the Bragg scattering theory, for a specific radar frequency band, the empirical geophysical model function (GMF) can be used to estimate the NRCS backscattered from sea surface more accurately (Verspeek et al., 2012; Li and Lehner, 2014; Mouche and Chapron, 2015; Shao et al., 2016).

In recent years, the numerical methods were also employed to investigate the Doppler spectra of backscattering from one-dimensional sea surfaces (Toporkov and Brown, 2000; Johnson et al., 2001; Hayslip et al., 2003). At low grazing angles (LGA), Toporkov et al. found that the results of numerical simulations showed an obvious broadening of the bandwidth for nonlinear surfaces and a separation of the vertical and horizontal polarization spectra (Toporkov and Brown, 2000). But for the linear sea surface, this spectral separation cannot be observed. Further, the influences of the hydrodynamic models on the Doppler spectra of L-band backscattered fields have been discussed by Johnson and Hayslip et al. (Johnson et al., 2001; Hayslip et al., 2003). In spite of the advantages of the numerical methods, several questions should be mentioned as following: on the one hand, in order to obtain exact numerical results, Doppler simulations turn out to be quite computationally expensive; on the other hand, the influences of different factors, such as hydrodynamic modulation, tilt modulation of large scale waves and so on cannot be assessed individually.

In addition to the theoretical and the numerical methods, a serious of the empirical Geophysical Model Functions (GMF) based on the Doppler shift observations combined with wind and sea state information have been developed in recent studies. For instance, a C-band empirical geophysical model function (CDOP) has been built for estimating wave-induced Doppler shift (Mouche et al., 2012). On the basis of the observed Doppler shift by Sentine-l SAR, another empirical geophysical model, called CDOP-3S which combined wave information into the model, was established by Moiseev et al. (2020). However, the CDOP-3S model performs an overfit of the empirical GMF during training. A new GMF called CDOP-3SiX has been trained based on the coastal data set in Moiseev et al. (2022). Due to addition of the sea wind and swell information, the CDOP-3SiX improves the accuracy of sea state contribution estimates compared to CDOP model. Although the development of the empirical geophysical model function can significantly facilitate the application of the Doppler information in ocean remote sensing. However, the accurate of the empirical geophysical model depends on the sensor's performance and optimal instrumental configurations. In addition, the empirical models are not easily used to analyze the physical mechanisms that affect the Doppler properties.

To progress in such investigations, our purpose in this paper is to numerically evaluate the wind induced Doppler shift of the echoes backscattered from sea surface by combining the TSM model and nonlinear sea wave model. Predictions will help to better understand the influence mechanism of incidence angle, polarization sensitivities, and modulation effects of large scale waves. What's more, in this study, the scattering coefficient in the TSM is calculated by the empirical CSAR model (Mouche and Chapron, 2015) rather than Bragg model to get more accurate results. Numerical results show that the Doppler shift of the C-band sea echoes at moderate incidence angles can be well predicted by the method in this work. In order to facilitate the application, a semi-empirical CSAR-DOP model is also developed based on the predicted Doppler shift in this work. In the following section, the numerical theory for Doppler shift is presented in Section II. The results of the numerical models are analyzed in Section III. Using the predicted Doppler shift, a polynomial fitting formula (CSAR-DOP model) is developed in Section IV. The concluding remarks and perspectives are provided in Section V.

2 The Doppler shift predicted by TSM

2.1 *The two-scale scattering model*

As the most practical model for theoretical description of microwave Doppler spectrum from sea surface, the two- scale model can be used to give a qualitative and quantitative interpretation of the Doppler shift. In TSM model, sea surface is artificially partitioned into small- and large-scale waves, such that

$$Z(x,y,t) = Z_l(x,y,t) + Z_s(x,y,t), \tag{1}$$

where x, y and t are spatial (horizontal and vertical) and time coordinates, respectively. $Z_l(x,y,t)$ represents the large-scale portion of the surface elevation. $Z_s(x,y,t)$, which has been modulated by large-scale waves, denotes small-scale roughness with $2k_e\cos\theta_i Z_s(x,y,t) \ll 1.0$. k_e is the wave number of microwave and θ_i denotes the incidence angle. If we assume that $Z_l(x,y,t)$ and $Z_s(x,y,t)$ are statistically independent, the total wave-height spectrum, i.e., $W(\boldsymbol{K})$, can be written as

$$W(\boldsymbol{K}) = W_{ms}(\boldsymbol{K}) + W_l(\boldsymbol{K}), \tag{2}$$

where $W_{ms}(\boldsymbol{K})$ and $W_l(\boldsymbol{K})$ denote the wave-height spectra corresponding to small- and large-scale surface roughness. In this work, the two-dimensional spectrum proposed by Elfouhaily et al. (1997) is selected for the large-scale sea waves.

According to the linear theory, the sea surface can be described as a sum of large number of harmonics with different amplitudes, frequencies, and random phases. However, if we aim at studying radar Doppler character, the nonlinearities of actual sea surface cannot be neglected, especially, the skewness properties would induce obvious effect on the Doppler shift. In general, the nonlinear sea surface can be expanded in perturbation series. The first order perturbation term corresponds to the linear surface and the higher order corrections come from the expansion of the hydrodynamic formulas in terms of wave interactions. For large-scale waves, the narrow-band assumption is acceptable. On the basis of this narrow band assumption, Tayfun (1986) proposed a nonlinear sea surface model, which results in a random sea surface whose crests are narrow and peaked, and whose troughs are long and flat. Such asymmetry of the vertical direction is referred to as vertical-skewness. At the same time, the horizontal-skewness, which directly affects the surface slope distribution, also occurs in sea waves. In Fung (1994), Fung found that, compared to vertical-skewness, the horizontal-skewness induces

more remarkable influence on backscattered signal. The Lagrange Model with linked components (hereinafter referred to as LMLC) is an optional hydrodynamic model for the nonlinear water waves (Lindgren, 2009; Lindgren and Åberg, 2009). The LMLC model can produce the realistic vertical- and horizontal-skewness. For two-dimensional deep water waves, the LMLC can be written as

$$Z_l(x,y,t)=\sum_{m=-M/2}^{M/2-1}\sum_{n=-N/2}^{N/2-1}F\left(K_{xm},K_{yn}\right)\times \exp\left[\mathrm{i}\left(K_{xm}x_0+K_{yn}y_0\right)-\mathrm{i}\omega_{mn}t\right], \tag{3}$$

with

$$\begin{aligned}x=&x_0-\sum_{m=-M/2}^{M/2-1}\sum_{n=-N/2}^{N/2-1}\mathrm{i}\frac{K_{xm}}{K_{mn}}F(K_{xm},K_{yn})\exp[\mathrm{i}(K_{xm}x_0+\\ &K_{yn}y_0)-\mathrm{i}\omega_{mn}t]+\sum_{m=-M/2}^{M/2-1}\sum_{n=-N/2}^{N/2-1}\alpha_{mn}\frac{K_{xm}}{K_{mn}}F(K_{xm},K_{yn})\times\\ &\exp[\mathrm{i}(K_{xm}x_0+K_{yn}y_0)-\mathrm{i}\omega_{mn}t],\end{aligned} \tag{4}$$

$$\begin{aligned}y=&y_0-\sum_{m=-M/2}^{M/2-1}\sum_{n=-N/2}^{N/2-1}\mathrm{i}\frac{K_{yn}}{K_{mn}}F(K_{xm},K_{yn})\exp[\mathrm{i}(K_{xm}x_0+\\ &K_{yn}y_0)-\mathrm{i}\omega_{mn}t]+\sum_{m=-M/2}^{M/2-1}\sum_{n=-N/2}^{N/2-1}\alpha_{mn}\frac{K_{yn}}{K_{mn}}F(K_{xm},K_{yn})\times\\ &\exp[\mathrm{i}(K_{xm}x_0+K_{yn}y_0)-\mathrm{i}\omega_{mn}t],\end{aligned} \tag{5}$$

where x_0 and y_0 are the abscissa and ordinate of the water particle's equilibrium position. And $F\left(K_{xm},K_{yn}\right)$ denotes the Fourier coefficients of sea surface profile, the wavenumber and the angular frequency are $K_{mn}=\sqrt{K_{xm}^2+K_{yn}^2}\leqslant K_{\mathrm{cut}}$ and $\omega_{mn}=\sqrt{gK_{mn}}$ with $K_{xm}=2\pi\left(m-M/2\right)/L_x$, $K_{yn}=2\pi(n-N/2)/L_y$. K_{cut} denotes the cut-off wavenumber. L_x and L_y are the lengths of sea surface along $\hat{x}$ and $\hat{y}$ directions, $m=1,2,\cdots,M$; $n=1,2,\cdots,N$. The linking parameter $\alpha_{mn}=\gamma/\omega_{mn}^2$, and γ can be defined by the relation between the horizontal acceleration of the water particles and the vertical displacement (Lindgren, 2009; Lindgren and Åberg, 2009).For narrow-band waves, $\gamma=0$ and $\gamma=\omega_{mn}^2$ correspond to the nonlinear sea surface models proposed in Tayfun (1986) and Chen et al.(1993), respectively. In Lindgren and Åberg (2009) and Lindgren (2009), Lindgren set $\gamma=0.4$ or 0.8 for horizontal-skewness water waves. However, strong correlation between the biphase $\beta_{mn}=\arctan\left(\gamma/\omega_{mn}^2\right)$ and wind forcing was found by Leykin et al. (1995) through the experiment in a laboratory wave tank under varied wind conditions. But, so far, few data measured from actual situation can be directly compared with the results obtained by Leykin and Donelan et al. (Leykin et al., 1995). In this work, we set $\gamma=0.4$. Because the difference of the orbital velocity for linear and nonlinear large scale waves only has negligible influence on the Doppler properties, for simplicity, the orbital velocity components in different directions are still simulated based on the linear wave model, i.e.,

$$V_z=-\sum_{m=-M/2}^{M/2-1}\sum_{n=-N/2}^{N/2-1}\mathrm{i}\omega_{mn}F(K_{xm},K_{yn})\exp[\mathrm{i}(K_{xm}x+K_{yn}y)-\mathrm{i}\omega_{mn}t], \tag{6}$$

$$V_x=\sum_{m=-M/2}^{M/2-1}\sum_{n=-N/2}^{N/2-1}\omega_{mn}\frac{K_{xm}}{K}F(K_{xm},K_{yn})\exp[\mathrm{i}(K_{xm}x+K_{yn}y)-\mathrm{i}\omega_{mn}t], \tag{7}$$

$$V_y=\sum_{m=-M/2}^{M/2-1}\sum_{n=-N/2}^{N/2-1}\omega_{mn}\frac{K_{yn}}{K}F(K_{xm},K_{yn})\exp[\mathrm{i}(K_{xm}x+K_{yn}y)-\mathrm{i}\omega_{mn}t]. \tag{8}$$

The small-scale roughness of sea waves would be modulated by the large-scale underlying waves, and the spatial variation of $W_{ms}(\boldsymbol{K})$ induced by the hydrodynamic modulation of large-scale waves can be written as

$$W_{ms}(\boldsymbol{K})=W_s(\boldsymbol{K})\left\{1+\sum_{m=-M/2+1}^{M/2}\sum_{n=-N/2+1}^{N/2}M_{\mathrm{hydr}}F(K_{xm},K_{yn})\times \exp[\mathrm{i}(K_{xm}x+K_{yn}y)-\mathrm{i}\omega_{mn}t]\right\}, \tag{9}$$

where $W_s(\boldsymbol{K})$ denotes the roughness spectrum which is not modulated by large-scale waves. And the hydrodynamic modulation transfer function M_{hydr} takes the form as Alpers et al. (1981),

$$M_{\mathrm{hydr}}=4.5\left|\boldsymbol{K}_l\right|\omega\frac{\omega-\mathrm{i}\mu}{\omega^2+\mu^2}\cos^2\left(\boldsymbol{K}_l,\boldsymbol{K}_s\right), \tag{10}$$

where $\boldsymbol{K}_l$ and $\boldsymbol{K}_s$ denote the wavenumbers of large- and small-scale waves, respectively. μ is the relaxation rate and has to be determined by experiment. For $\mu=0$, the maximum of the short wave energy occurs at the crests of the large-scale waves. However, the fact is that a nonvanishing phase shift between the maximum of the short wave spectral energy and the large-scale waves' crest exists, which yields a different scattering coefficient when radar looks along the upwind and downwind directions. As discussed in Wang et al. (2016), the hydrodynamic modulation of large-scale waves is more significant with wind speed. Thus a reasonable Doppler shift could be obtained by relating the wind speed to the relaxation rate μ, characterized by setting the nonvanishing phase shift to be about $\pi/4$ (i.e., $\mu=\omega_p$), representing the angle frequency of the spectral peak wave. Thus, based on the two-scale model, the scattering coefficient from each facet on the large scale waves can be expressed as

$$\sigma_{\mathrm{pp}}(\theta_i')\approx\overline{\sigma_{\mathrm{pp}}(\theta_i')}\left\{1+\sum_{m=-M/2+1}^{M/2}\sum_{n=-N/2+1}^{N/2}M_{\mathrm{hydr}}F\left(K_{xm},K_{yn}\right)\times \exp\left[\mathrm{i}\left(K_{xm}x+K_{yn}y\right)-\mathrm{i}\omega_{mn}t\right]\right\}. \tag{11}$$

In the traditional two-scale model, the scattering coefficient $\overline{\sigma_{\mathrm{PP}}(\theta_i')}$ in Eq. (11) is evaluated by the Bragg theory. However, as an analytical approximation method, the Bragg resonance scattering method cannot accurately describe the backscattering field from sea surface. Therefore, in the present work, the dual-polarized C-band empirical geophysical model function (CSAR model) (Mouche and Chapron, 2015) is employed to evaluate the scattering coefficient $\overline{\sigma_{\mathrm{PP}}(\theta_i')}$. The subscript PP represents HH or VV polarization. The local incidence angle $\theta_i'\approx\theta_i-S_l$, θ_i is the incidence angle, the slope of the large scale waves along radar

look direction is

$$S_l = S_x \cos\varphi_i + S_y \sin\varphi_i = \frac{\partial Z_l}{\partial x}\cos\varphi_i + \frac{\partial Z_l}{\partial y}\sin\varphi_i, \quad (12)$$

where φ_i denotes the azimuth angle of the radar beam (i.e., the angle between radar beam direction and x-axis direction).

2.2 *The Doppler centroid frequency shift*

Doppler centroid frequency shift (f_D) can be generally considered as the first-order moment of Doppler spectrum and weighted by scattering power. First of all, at moderate incidence angles, the microwave scattering field from sea surface is dominated by resonant Bragg scattering, thus the phase speed of the short Bragg resonant water waves would yield a partial Doppler shift. Accordingly, the corresponding Doppler spectrum would consist of two spectral peaks resulting from the phase speed of the Bragg wave components traveling toward and away from radar. However, under actual sea conditions, these spectral peaks are not only broadened but also shifted due to the modulation effect of the large-scale waves. Considering the effect of the tilt and the hydrodynamic modulation of the large-scale waves, the additional Doppler centroid frequency shift (f_M) can be evaluated by

$$f_M = \frac{\sum_{m=-M/2+1}^{M/2}\sum_{n=-N/2+1}^{N/2}\sigma_{PP}(\theta'_i) f_{mn}}{\sum_{m=-M/2+1}^{M/2}\sum_{n=-N/2+1}^{N/2}\sigma_{PP}(\theta'_i)}, \quad (13)$$

with

$$f_{mn} = \frac{k_e}{\pi}(V_{zmn}\cos\theta_i + V_{xmn}\sin\theta_i\cos\varphi_i + V_{ymn}\sin\theta_i\sin\varphi_i), \quad (14)$$

where the velocities V_{xmn}, V_{ymn} and V_{zmn} can be evaluated by Eqs (6)–(8). Based on the Bragg scattering and the modulation of Bragg waves by longer waves, the Doppler centroid frequency shift of the microwave echoes backscattering from sea surface can be written as

$$f_D = f_M + f_B + f_{drift}, \quad (15)$$

with

$$f_{drift} = \frac{1}{2\pi}\boldsymbol{U}_{drift}\cdot\boldsymbol{K}_B, \quad (16)$$

$$f_B = \frac{1}{2\pi}\sqrt{g|\boldsymbol{K}_B(\theta_i)|}\left[F(K_B,\phi_B) + F(K_B,\phi_B+\pi)\right], \quad (17)$$

where the wind drift $\boldsymbol{U}_{drift} = 0.03\boldsymbol{U}_{10}$ and $\boldsymbol{U}_{10}$ denotes the wind speed at a height of 10 m above sea surface. $\boldsymbol{K}_B$ is the wave number of Bragg wave, ϕ_B denotes the azimuth angle of the Bragg wave. $F(K,\phi)$ denotes the angle spread function (Apel, 1994).

From Eqs (13) and (14) we can find that the predicted Doppler centroid frequency shift would be affected by the locally-modulated radar cross section and the orbital motions of the large-scale waves. Figure 1 illustrates the simulated profiles of the nonlinear surface and the linear surface. Here, the wind speed is U_{10}=12 m/s. From Fig. 1, it can be seen that the main differences between nonlinear and linear profiles are in the crests and troughs. The nonlinear sea surface profile has flattened troughs and narrower peaks. In addition, for the nonlinear sea surface profile, the crests tilt in the downwind direction. Meanwhile, the tilt and the hydrodynamic modulations of the scattering coefficient and the radar line-of-sight velocity of the scattering facets are also presented in Fig. 1. If the large-scale waves propagate towards the radar, the scattering facets with positive slope generally generate higher scattering intensity and move closely to the radar. On the contrary, the scattering facets with negative slope generate lower scattering intensity and move away from the radar. Further, because the small-scale roughness is modulated by the hydrodynamic modulation of the large-scale waves, as shown in Fig. 1, the scattering intensity would also be modulated by the hydrodynamic modulation. When the effect of the hydrodynamic modulation with a relaxation rate μ=0 is considered, the scattering coefficient becomes larger at the crests of the large-scale waves. If the value of the relaxation rate is set to be ω_p, as shown in Fig. 1, the modulated scattering coefficient becomes larger at the front of the wave crests. The asymmetries of the scattering intensity induced by the tilt and the hydrodynamic modu-

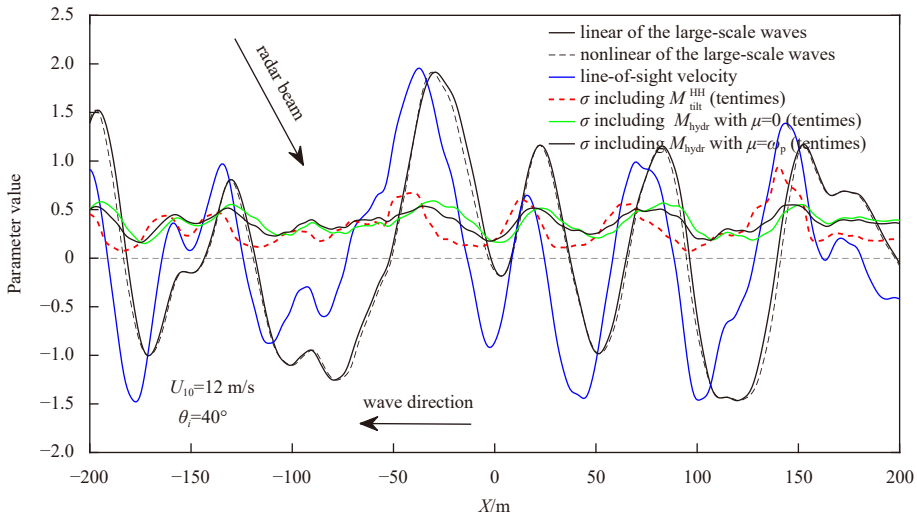

Fig. 1. The profile and the line-of-sight velocity of the large-scale sea waves, as well as the modulated scattering coefficient. For comparison, the value of the scattering coefficient has been enlarged 10 times.

lations in Fig. 1 would induce an additional Doppler shift.

3 Numerical results and discussion

In the two-scale model, how to set the cut-off wavenumber K_{cut} should be noted. In Fig. 2, the predicted Doppler shifts with different cut-off wavenumbers are presented. Here, the incidence angle $\theta_i = 40°$ and the wind speed U_{10}=10 m/s, and the scattering coefficient is evaluated by the empirical CSAR model. The curves in Fig. 2 show that the absolute values of the Doppler shifts increases with the cut-off wavenumbers until its value up to $K_B/20$. When the cut-off wavenumber is higher than $K_B/20$, the predicted Doppler shift for both polarizations tend to be constant. Therefore, in our work, we perform the simulation of the large-scale waves with the cut-off wavenumber $K_{cut} = K_B/20$.

In upwind and downwind directions, the influences of the incidence angle on the Doppler shifts predicted by the TSM are presented in Fig. 3. When the wind speed is 10 m/s, the absolute value of the Doppler shift in upwind direction is always larger than that in downwind direction within the range of medium incidence angle. The numerical results in Wang et al. (2012) showed that the horizontal-skewness of the large-scale waves would induce this difference. As shown in Fig. 1, the scattering coefficient from the local water surface would be modulated by the tilt and the hydrodynamic modulations of the large-scale waves. Because Doppler shifts are weighted by the power of the scattering field, thus the tilt and the hydrodynamic modulations would induce effects on the difference between the absolute values of the Doppler shifts in upwind and downwind directions. The curves in Wang et al. (2016) (Fig. 4 in Wang et al. (2016)) demonstrate that the value of the Doppler shift difference between upwind and downwind directions varies regularly with the relaxation rate for various wind speeds. With the increase of the relaxation rate, this difference gradually increases firstly until reaching the max maximum value, and then decreases with a relative smaller rate. Up to now, however, the relaxation rate is poorly known experimentally. Moreover, the values estimated by various investigators differ by almost one order of magnitude (Caponi et al., 1988). In Caponi et al. (1988), for moderate wind speeds, the value of the relaxation rate is 0.1 s^{-1} for L-band radar wave, and 1.7 s^{-1} for X-band radar wave. For C-band radar wave, the relaxation rate obtained by interpolating the values corresponding to L-band and X-band microwaves is 0.92 s^{-1}, which is close to the angular frequency ω_p of the dominate wave. Therefore, in this work, the value of the relaxation rate is set to be ω_p.

For comparisons, the predicted Doppler shifts when the CSAR model is replaced by the traditional Bragg scattering coefficient are also shown in Fig. 3. In the incidence angle range of 25° to 45°, the absolute values of the Doppler shifts for upwind and downwind directions decrease with the incidence angle. Moreover, the Doppler shifts based on the CSAR model are usually larger than those obtained based on the traditional Bragg theory, except at smaller or larger incidence angles for HH-polarization case. In order to further explain the reason for the difference between the Doppler shifts corresponding to the experimental CSAR model and the traditional Bragg theory, the tilt modulation-transfer functions (MTFs) evaluated by CSAR model

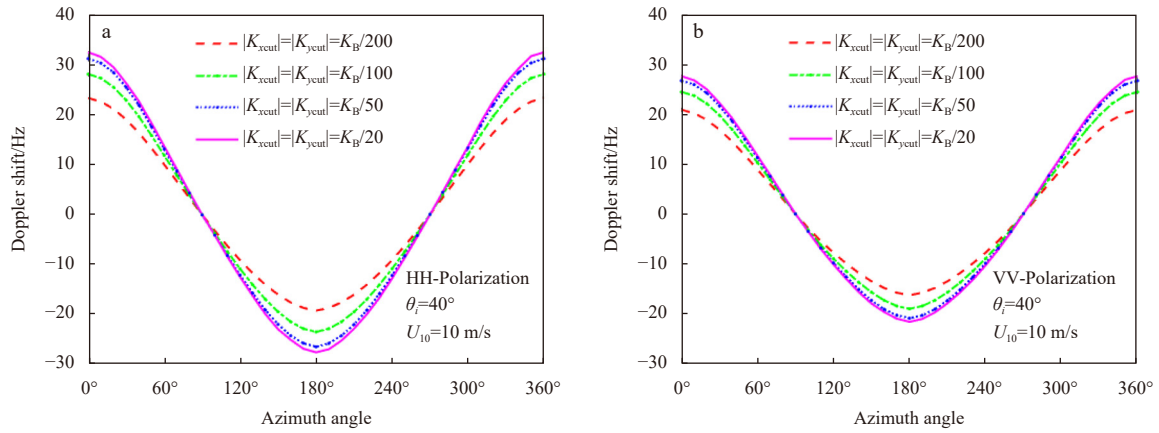

Fig. 2. The influence of the cut-off wavenumber on the predicted Doppler shift.

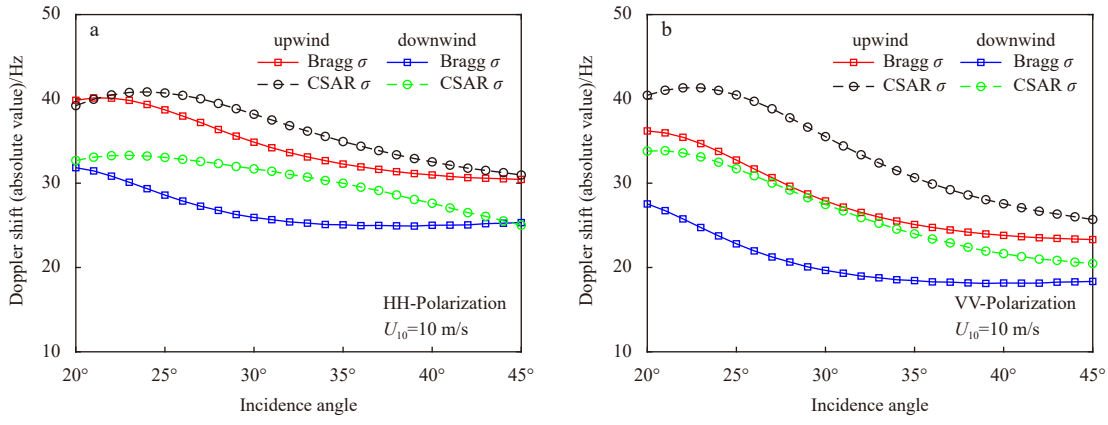

Fig. 3. The absolute values of the Doppler shift predicted by the two-scale surface scattering model with respect to incidence angle for upwind and downwind directions by using different scattering coefficient: Bragg model and CSAR model.

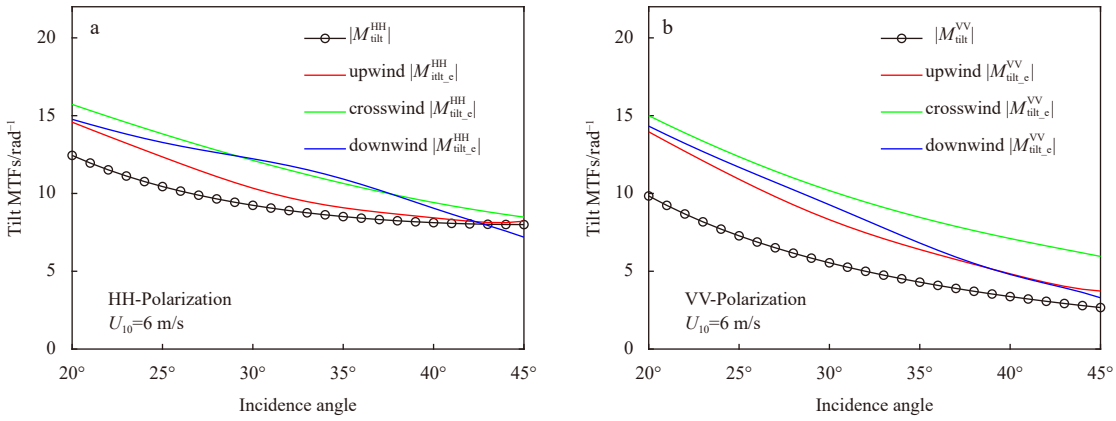

Fig. 4. Theoretical tilt modulation-transfer functions (MTFs) and experimental tilt MTFs with respect to incidence angle at 6 m/s wind speed.

and by Bragg theory are shown in Fig. 4. Here, the experimental tilt MTFs for the CSAR model are calculated by

$$M_{\rm tilt\_e}^{\rm HH}(\boldsymbol{U},\theta_i,\phi_i)=\mathrm{i}k_l\frac{1}{\sigma_{\rm HH}^{e}(\boldsymbol{U},\theta_i,\phi_i)}\frac{\partial\sigma_{\rm HH}^{e}}{\partial\theta}\bigg|_{\theta=\theta_i,\ \phi=\phi_i}, \tag{18}$$

and

$$M_{\rm tilt\_e}^{\rm VV}(\boldsymbol{U},\theta_i,\phi_i)=\mathrm{i}k_l\frac{1}{\sigma_{\rm VV}^{e}(\boldsymbol{U},\theta_i,\phi_i)}\frac{\partial\sigma_{\rm VV}^{e}}{\partial\theta}\bigg|_{\theta=\theta_i,\ \phi=\phi_i}. \tag{19}$$

where $\sigma_{\rm PP}^{e}$ represents empirical scattering coefficient.

The theoretical tilt MTFs derived based on the Bragg resonance theory for HH and VV polarizations are written as (Lyzenga, 1986; Hasselmann and Hasselmann, 1991)

$$M_{\rm tilt}^{\rm HH}=8\mathrm{i}k_l(\sin 2\theta)^{-1}, \tag{20}$$

and

$$M_{\rm tilt}^{\rm VV}=4\mathrm{i}k_l\cot\theta(1+\sin^2\theta)^{-1}. \tag{21}$$

In order to make the theoretical tilt MTFs and the experimental tilt MTFs comparable, in Fig. 4, the values of the tilt MTFs have been normalized with $\mathrm{i}k_l$. First of all, the tilt modulations for both the Bragg theory and the CSAR model decrease with incidence angle. This phenomenon means that the weight effect of the scattering coefficient due to sea surface slope becomes weaker with the increase of the incident angle. And then, the absolute values of the Doppler shift in Fig. 3 would also decrease with the incidence angle. From the comparisons between the theoretical tilt MTFs with the experimental tilt MTFs, we also find that the values of the experimental tilt MTFs are usually larger than those of the theoretical tilt MTFs. Therefore, the Doppler shift corresponding to the CSAR model are usually larger than those corresponding to the traditional Bragg theory. In addition, from Eqs (20) and (21) we can find that the theoretical tilt MTFs for both HH and VV polarizations have nothing to do with wind speed and wind direction. However, the curves in Fig. 4 show that the experimental tilt MTFs becomes the largest when radar looks along crosswind direction, while it has the smallest value when radar looks along upwind direction. These properties of the experimental tilt MTFs would induce somewhat effect on the predicted Doppler shift. The difference between the theoretical and the experimental tilt MTFs mentioned above means that it is necessary to apply the CSAR model rather than the Bragg scattering model.

The effects of different factors on the predicted Doppler shift are presented in Fig. 5. From the results we can find that the Doppler shifts due to the phase velocity of the Bragg of resonant wave, surface drift current, as well as the hydrodynamic modulation of large-scale waves have nothing to do with radar polarization. However, the Doppler shifts caused by the tilt modulations are significantly influenced by radar polarization. And the abso-

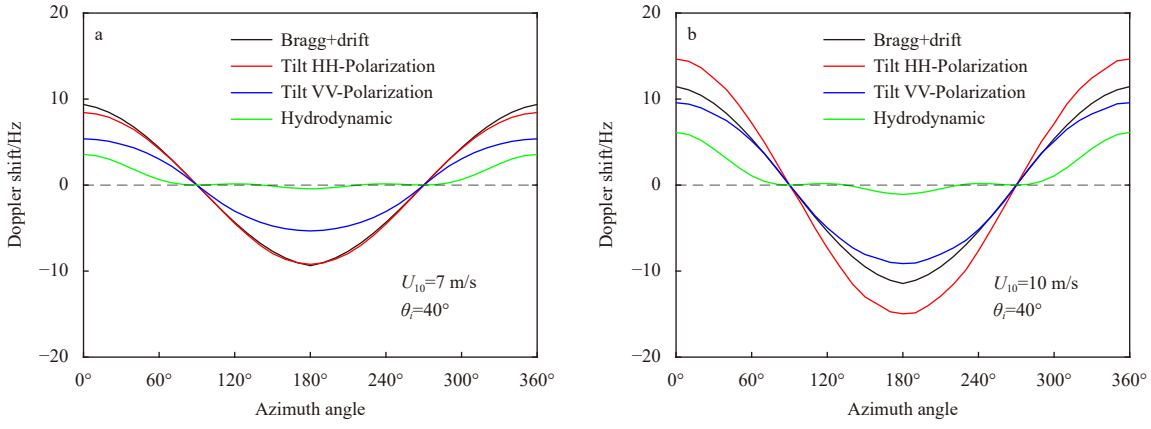

Fig. 5. The effects of different factors on Doppler shift at different wind speeds. a. U_{10}=7 m/s; b. U_{10}=10 m/s.

lute value of Doppler shift for HH polarization is obvious larger than that corresponding to VV polarization. These differences can be attributed to the fact that the radar signals in HH polarization are more sensitive to the slope of large scale waves than in VV polarization. The comparison between the curves in Figs 5a and b demonstrate that the absolute values of the predicted Doppler shift corresponding to each factor increases with wind speed. On the other hand, the predicted Doppler shifts are all sensitive to the azimuth angle. As anticipated, when the azimuth angle of the radar beam is 90° or 270° (the cross-wind direction), the Doppler shifts due to different factors are all equal to zero, when the radar beam is directed toward the wind direction (upwind), the Doppler shifts are positive whereas they change sign under downwind conditions. Meanwhile, the Doppler shifts corresponding to the tilt and the hydrodynamic modulations show the asymmetries between upwind and downwind observations.

In order to verify Doppler shift predicted by the TSM model with, the Doppler centroid frequency shift predicted by the CDOP (Mouche et al., 2012), which is an empirical model for C-band echoes backscattered from sea surface, are also given out for comparison in Figs 6 and 7. In Fig. 6, the wind speed is 10 m/s. At different incidence angles, from the comparisons we can find that the predicted Doppler shifts by the TSM are generally in good agreement with the CDOP predictions. What's more, the TSM model with σ_{Bragg} underestimates the frequency shift results slightly compared to TSM model with σ_{CSAR} and CDOP results. In Fig. 8, the comparisons between the TSM and the CDOP are shown for different wind speeds. The absolute values of the Doppler shifts predicted by the TSM model at a low wind speed are somewhat smaller than those predicted by the CDOP model. Meanwhile, from the results in Figs 6 and 7 we can find that the Doppler shifts for HH polarization predicted by the CDOP model are suddenly reduced in the windward direction around the upwind direction (azimuth angle is 0° or 360°). This phenomenon is difficult to explain physically. Moreover, when wind speed is higher, the CDOP model perhaps underestimates the Doppler shift of the VV polarized echoes at downwind direction (as shown in Fig. 7d). In order to further analyze the difference of the Doppler shifts predicted by the TSM and the CDOP models, the predicted Doppler shifts at upwind and downwind directions as functions of wind speed are shown in Fig. 8. With the decrease of wind speed, the values of the predicted Doppler shifts by the TSM model for both polarizations tend to be consistent with each other, however, this phenomenon is not clearly shown in the results of the CDOP model. Meanwhile, the Doppler shifts predicted by the TSM model at lower (higher) wind speed are smaller (larger) than those predicted by the CDOP model.

Figure 9 shows the comparison of Doppler shift results between our model (TSM model), CDOP and an updated GMF CDOP-3SiX (Moiseev et al., 2022) for different wind speeds and wind directions between 0° (upwind) and 180° (downwind) at two incidence angle 36° (top row) and 44° (bottom row). By comparing the results between three models for 3 m/s wind speed (left column) at both 36° and 44° incidence angles, the values of our model are closer to the CDOP-3SiX model, comparatively, the CDOP model significantly overestimate the Doppler shifts results at such a low wind speed. When the wind speed is 6 m/s (middle column), the results of three models are similar. When the wind speed reaches 12 m/s (right column), the values of the

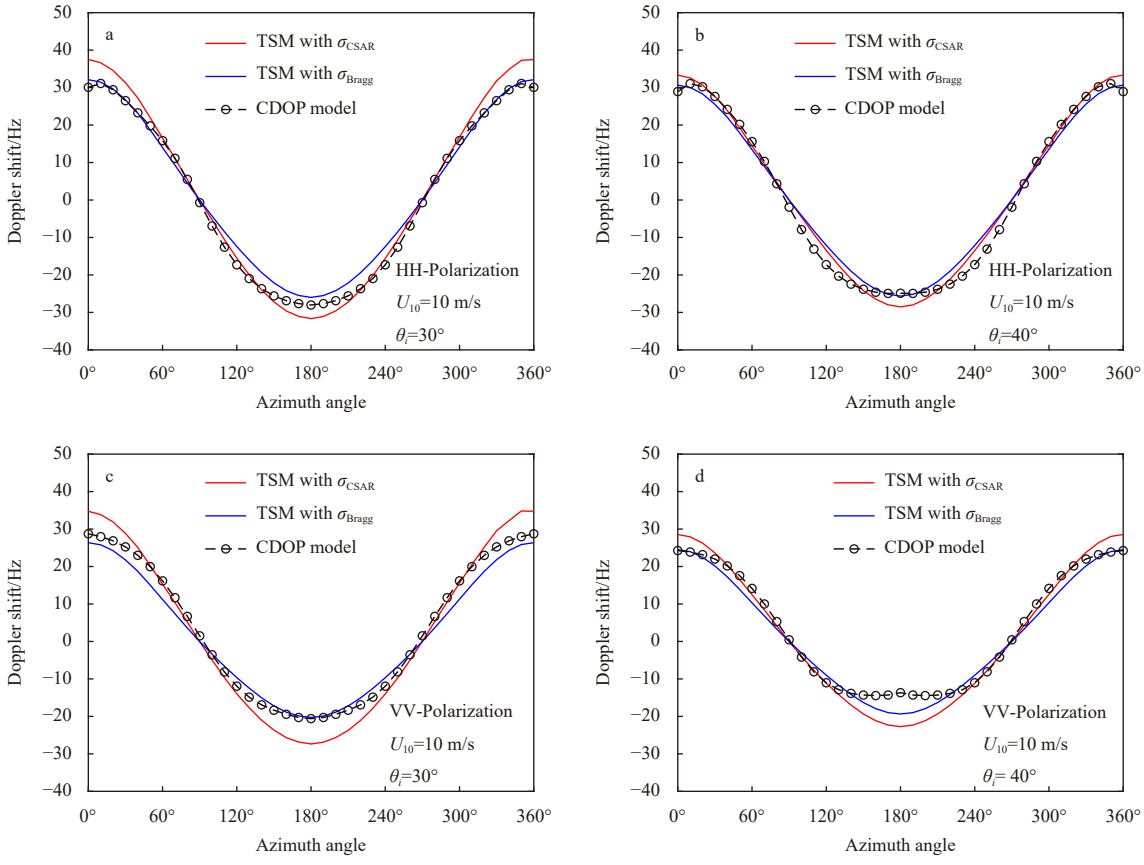

Fig. 6. Comparisons between the Doppler shift results evaluated by our model (two scale surface scattering model (TSM) with σ_{CSAR}), TSM with σ_{Bragg} and C-band empirical geophysical model function (CDOP) for different incidence angles.

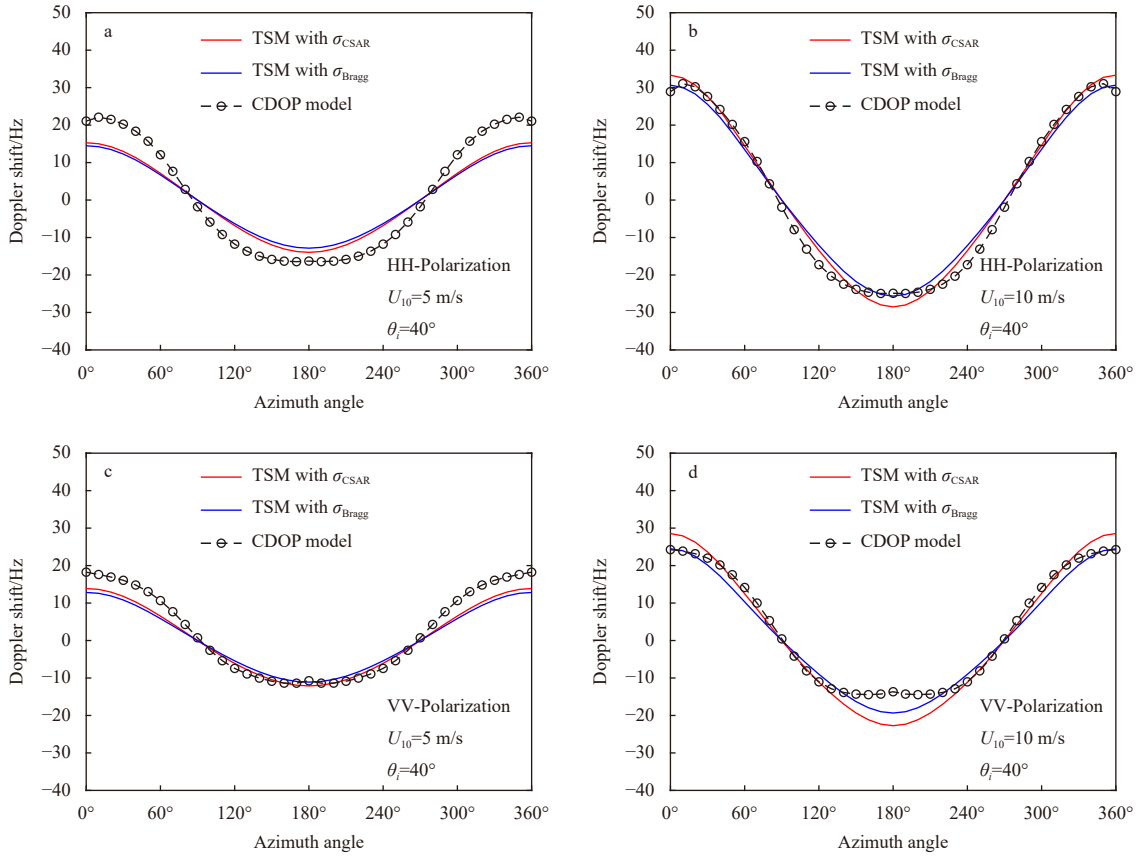

Fig. 7. Comparisons between the Doppler shift results evaluated by our model (two scale surface scattering model (TSM) with σ_{CSAR}), TSM with σ_{Bragg} and C-band empirical geophysical model function (CDOP) for different wind speeds.

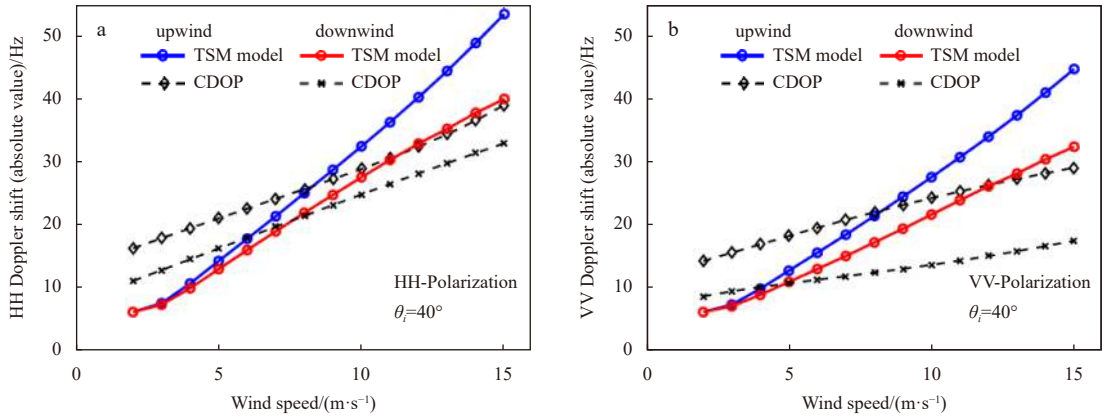

Fig. 8. Doppler shift as a function of wind speed for upwind and downwind at 40° incidence angle. TSM: two scale surface scattering model; CDOP: C-band empirical geophysical model function.

Doppler shift evaluated by our model near upwind and downwind directions are larger than the results of other two models, possibly because the modulations in the TSM model are somewhat larger than actual values at high wind speeds.

4 A fitting model for the predicted Doppler shift

In order to facilitate the application, a fitting model can be applied to give the function relation between the values of the Doppler shift and the incidence angle, wind speed and wind direction. The fitting formulas based on the Doppler shift predicted by numerical TSM model for HH and VV polarizations can be decomposed as a harmonic expressions (hereinafter referred to as CSAR-DOP), i.e.,

$$f_{\mathrm{D}}^{\mathrm{PP}}(\theta,\phi,U_{10}) = C_1^{\mathrm{PP}}(\theta,U_{10})\cos(\phi) + C_2^{\mathrm{PP}}(\theta,U_{10})(1+\cos(2\phi)), \tag{22}$$

where, the coefficients C_n^{PP} are related to the Doppler shift f_{D} in two main directions (upwind $\phi=0$ rad and downwind $\phi=\pi$ rad) by

$$C_1^{\mathrm{PP}}(\theta) = \frac{f_{\mathrm{D}}^{\mathrm{PP}}(\theta,0) - f_{\mathrm{D}}^{\mathrm{PP}}(\theta,\pi)}{2}, \tag{23}$$

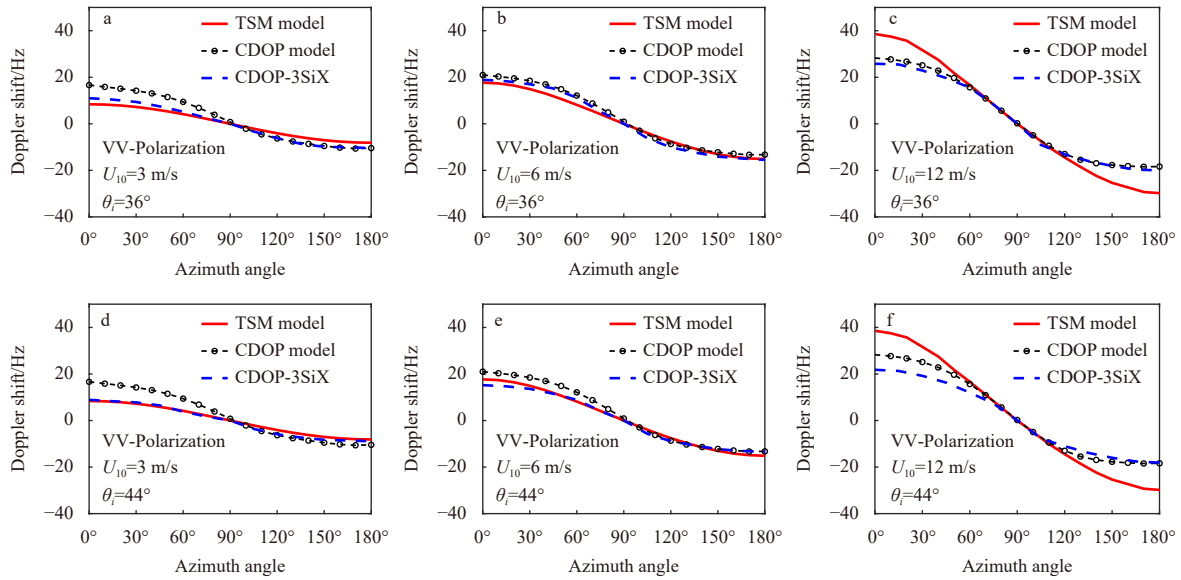

Fig. 9. The evaluation of the Doppler shift predicted using different models: C-band empirical geophysical model function (CDOP), CDOP-3SiX, and our model (two scale surface scattering model (TSM)) for different wind speeds and wind directions between 0° (upwind) and 180° (downwind) at two incidence angle 36° (top row) and 44° (bottom row). The dotted black line with circle in panel represents CDOP model from Mouche et al. (2012). The blue dotted line in panel represents CDOP3SiX model from Moiseev et al. (2022).

$$C_2^{\mathrm{PP}}(\theta) = \frac{f_{\mathrm{D}}^{\mathrm{PP}}(\theta,0) + f_{\mathrm{D}}^{\mathrm{PP}}(\theta,\pi)}{4}. \tag{24}$$

The polynomial fitting formulas of the coefficients C_n^{PP} for VV and HH polarizations are given out in Appendix when performed over all wind speeds between 2 m/s and 15 m/s, and all incidence angles between 20° and 45°. The values of the Doppler shift for HH and VV polarizations evaluated by the CSAR-DOP for different wind speeds are shown in Figs 10 and 11. The left pat-

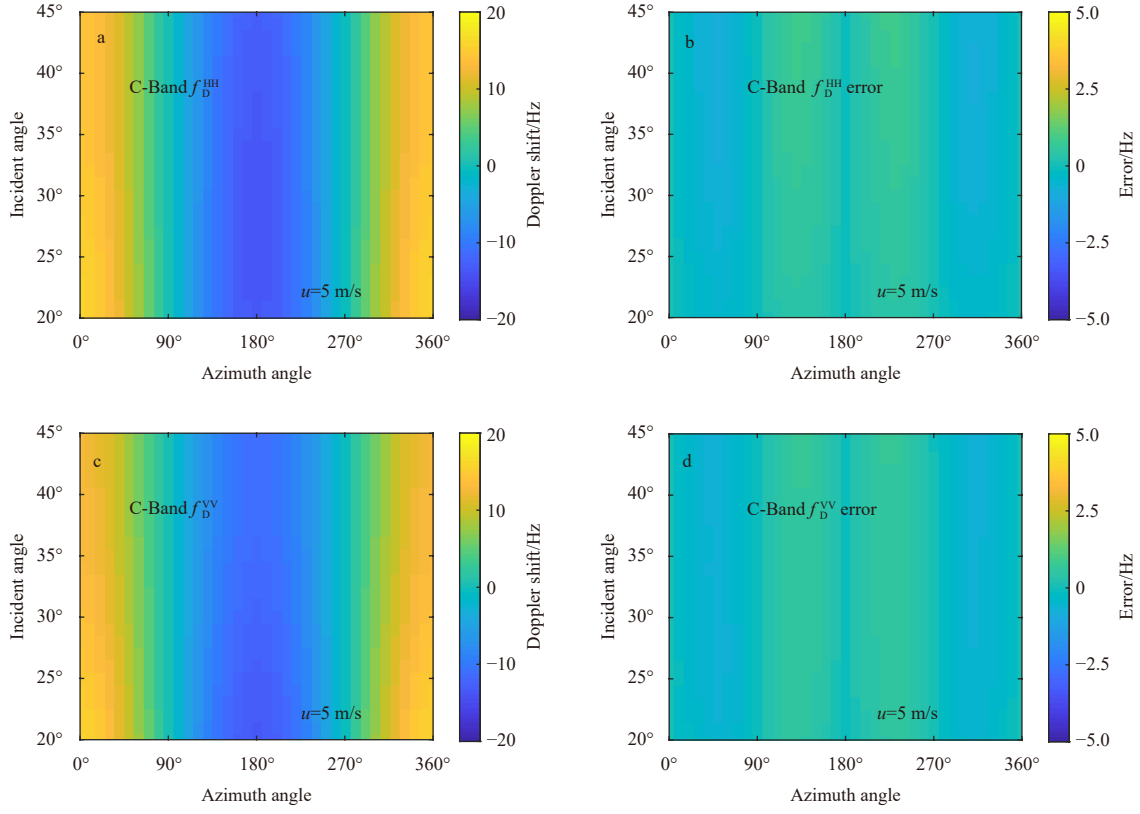

Fig. 10. Values of the Doppler shift evaluated by the fitting model for wind speed (u) of 5 m/s (left patterns) and the errors (right patterns).

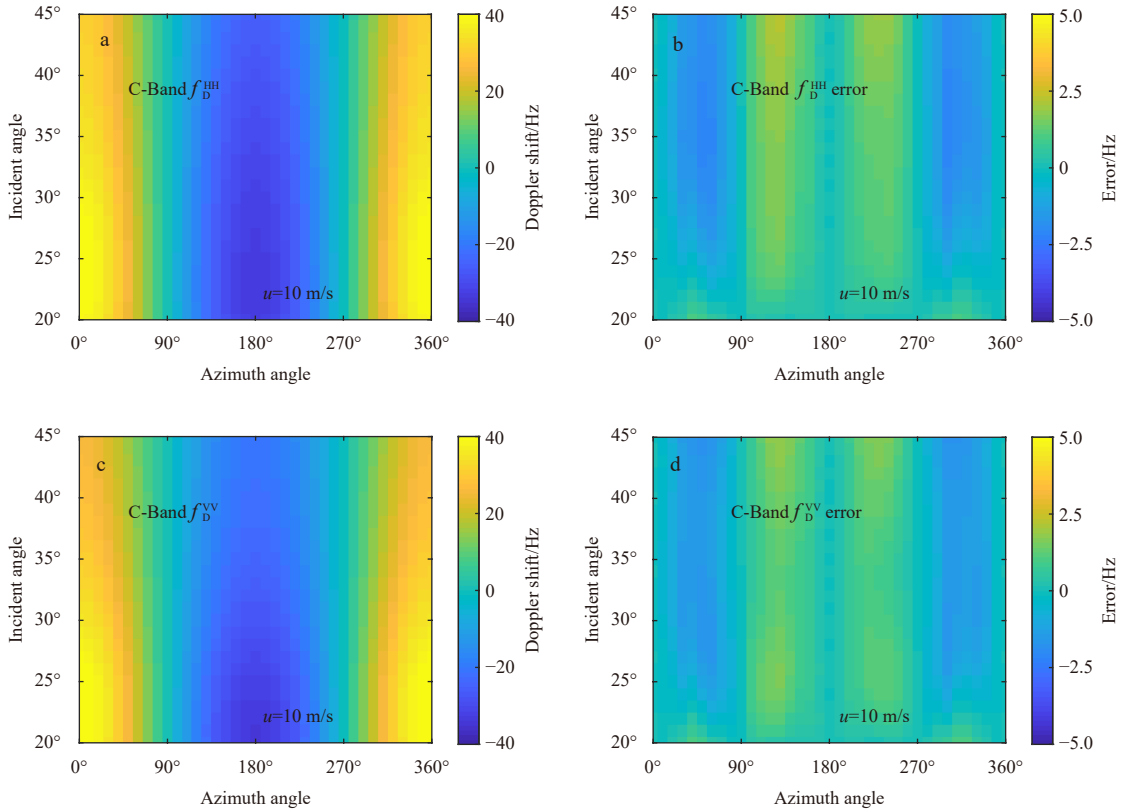

Fig. 11. Values of the Doppler shift evaluated by the fitting model for wind speed (u) of 10 m/s (left patterns) and the errors (right patterns).

terns of the figures show the values of the Doppler shift and the right patterns show the error between the Doppler shift predicted by TSM and that predicted by the CSAR-DOP. The small error in Figs 10 and 11 means that the CSAR-DOP model can be used to predict the Doppler shift.

5 Conclusions

In this work, we have presented a numerical method based on the TSM and nonlinear sea wave model for predicting the Doppler shift of C-band echoes backscattered from ocean surface at moderate incident angle. Based on the numerical method, the factors and the mechanisms affecting the Doppler frequency shift of sea surface echoes are analyzed in detail. From the predicted Doppler shifts, we can firstly find that the Doppler shifts would be obviously affected by the tilt modulation of the large scale waves. And the Doppler shift for HH polarization is always larger than that for VV polarization just due to the tilt modulation. Secondly, at moderate incidence angles, the difference between the Doppler shift predicted in upwind and downwind direction is mainly affected by the hydrodynamic modulation of the large-scale waves. Compared with the Doppler shift evaluated by the CDOP model, more reasonable Doppler shift at upwind and downwind directions can be predicted by the TSM model at lower wind speeds. Moreover, the Doppler shift results of TSM model under low wind speeds are also found to agree with the CDOP-3SiX. At the end of this work, to facilitate the application, the semi-empirical Doppler shift model (CSAR-DOP) for HH and VV polarization cases have been developed on the basis of the polynomial fitting method. The comparison between the Doppler shifts predicted by TSM and by CSAR-DOP illustrate that CSAR-DOP model can be used to predict the Doppler shift.

References

Alpers W R, Ross D B, Rufenach C L. 1981. On the detectability of ocean surface waves by real and synthetic aperture radar. Journal of Geophysical Research, 86(C7): 6481–6498, doi: 10.1029/JC086iC07p06481

Apel J R. 1994. An improved model of the ocean surface wave vector spectrum and its effects on radar backscatter. Journal of Geophysical Research, 99(C8): 16269–16291, doi: 10.1029/94JC00846

Barrick D E. 1977. Extraction of wave parameters from measured HF radar sea-echo Doppler spectra. Radio Science, 12(3): 415–424, doi: 10.1029/RS012i003p00415

Bass F G, Fuks I, Kalmykov A I, et al. 1968. Very high frequency radiowave scattering by a disturbed sea surface Part II: scattering from an actual sea surface. IEEE Transactions on Antennas and Propagation, 16(5): 560–568, doi: 10.1109/TAP.1968.1139244

Caponi E A, Crawford D R, Yuen H C, et al. 1988. Modulation of radar backscatter from the ocean by a variable surface current. Journal of Geophysical Research, 93(C10): 12249–12263, doi: 10.1029/JC093iC10p12249

Chapron B, Collard F, Ardhuin F. 2005. Direct measurements of ocean surface velocity from space: interpretation and validation. Journal of Geophysical Research, 110(C7): C07008

Chen K S, Fung A K, Amar F. 1993. An empirical bispectrum model for sea surface scattering. IEEE Transactions on Geoscience and Remote Sensing, 31(4): 830–835, doi: 10.1109/36.239905

Crombie D D. 1955. Doppler spectrum of sea echo at 13.66Mc./s. Nature, 175(4459): 681–682, doi: 10.1038/175681a0

Elfouhaily T, Chapron B, Katsaros K, et al. 1997. A unified directional spectrum for long and short wind-driven waves. Journal of Geophysical Research, 102(C7): 15781–15796, doi: 10.1029/97JC00467

Fuks I M, Voronovich A G. 2002. Radar backscattering from Gerstner's sea surface wave. Waves in Random Media, 12(3): 321–339, doi: 10.1088/0959-7174/12/3/305

Fung A K. 1994. Microwave Scattering and Emission Models and Their Applications. Norwood: Artech House

Hasselmann K, Hasselmann S. 1991. On the nonlinear mapping of an ocean wave spectrum into a synthetic aperture radar image spectrum and its inversion. Journal of Geophysical Research, 96(C6): 10713–10729, doi: 10.1029/91JC00302

Hayslip A R, Johnson J T, Baker G R. 2003. Further numerical studies of backscattering from time-evolving nonlinear sea surfaces. IEEE Transactions on Geoscience and Remote Sensing, 41(10): 2287–2293, doi: 10.1109/TGRS.2003.814662

Johannessen J A, Kudryavtsev V, Akimov D, et al. 2005. On radar imaging of current features: 2. Mesoscale eddy and current front detection. Journal of Geophysical Research, 110(C7): C07017

Johnson J T, Burkholder R J, Toporkov J V, et al. 2009. A numerical study of the retrieval of sea surface height profiles from low grazing angle radar data. IEEE Transactions on Geoscience and Remote Sensing, 47(6): 1641–1650, doi: 10.1109/TGRS.2008.2006833

Johnson J T, Toporkov J V, Brown G S. 2001. A numerical study of backscattering from time-evolving sea surfaces: comparison of hydrodynamic models. IEEE Transactions on Geoscience and Remote Sensing, 39(11): 2411–2420, doi: 10.1109/36.964977

Karaev V, Kanevsky M, Meshkov E. 2008. The effect of sea surface slicks on the Doppler spectrum width of a backscattered microwave signal. Sensors, 8(6): 3780–3801, doi: 10.3390/s8063780

Keller W C, Plant W J, Alenzuela G R. 1986. Observation of breaking ocean waves with coherent microwave radar. In: Phillips O M, Hasselmann K, eds. Wave Dynamics and Radio Probing of the Ocean Surface. Boston: Springer, 285–293

Kudryavtsev V, Akimov D, Johannessen J, et al. 2005. On radar imaging of current features: 1. Model and comparison with observations. Journal of Geophysical Research, 110(C7): C07016

Leykin I A, Donelan M A, Mellen R H, et al. 1995. Asymmetry of wind waves studied in a laboratory tank. Nonlinear Processes in Geophysics, 2(3): 280–289, doi: 10.5194/npg-2-280-1995

Li Xiaoming, Lehner S. 2014. Algorithm for sea surface wind retrieval from TerraSAR-X and TanDEM-X Data. IEEE Transactions on Geoscience and Remote Sensing, 52(5): 2928–2939, doi: 10.1109/TGRS.2013.2267780

Lindgren G. 2009. Exact asymmetric slope distributions in stochastic Gauss-Lagrange ocean waves. Applied Ocean Research, 31(1): 65–73, doi: 10.1016/j.apor.2009.06.002

Lindgren G, Åberg Sofia. 2009. First order stochastic Lagrange model for asymmetric ocean waves. Journal of Offshore Mechanics and Arctic. Engineering, 131(3): 031602

Lipa B. 1978. Inversion of second-order radar echoes from the sea. Journal of Geophysical Research, 83(C2): 959–962, doi: 10.1029/JC083iC02p00959

Lyzenga D R. 1986. Numerical simulation of synthetic aperture radar image spectra for ocean waves. IEEE Transactions on Geoscience and Remote Sensing, GE-24(6): 863–872, doi: 10.1109/TGRS.1986.289701

Moiseev A, Johannessen J A, Johnsen H. 2022. Towards retrieving reliable ocean surface currents in the coastal zone from the sentinel-1 Doppler shift observations. Journal of Geophysical Research, 127(5): e2021JC018201

Moiseev A, Johnsen H, Johannessen J A, et al. 2020. On removal of sea state contribution to Sentinel-1 Doppler shift for retrieving reliable ocean surface current. Journal of Geophysical Research, 125(9): e2020JC016288

Mouche A, Chapron B. 2015. Global C-Band Envisat, RADARSAT-2 and Sentinel-1 SAR measurements in copolarization and cross-polarization. Journal of Geophysical Research, 120(11): 7195–7207, doi: 10.1002/2015JC011149

Mouche A A, Chapron B, Reul N, et al. 2008. Predicted Doppler shifts induced by ocean surface wave displacements using asymptotic electromagnetic wave scattering theories. Waves in Random and Complex Media, 18(1): 185–196, doi: 10.1080/17455030701564644

Mouche A A, Collard F, Chapron B, et al. 2012. On the use of Doppler shift for sea surface wind retrieval from SAR. IEEE Transactions on Geoscience and Remote Sensing, 50(7): 2901–2909, doi: 10.1109/TGRS.2011.2174998

Shao Weizeng, Zhang Zheng, Li Xiaoming, et al. 2016. Sea surface wind speed retrieval from TerraSAR-X HH polarization data using an improved polarization ratio model. IEEE Journal of Selected Topics in Applied Earth Observations and Remote Sensing, 9(11): 4991–4997, doi: 10.1109/JSTARS.2016.2590475

Tayfun M A. 1986. On narrow-band representation of ocean waves: 1. Theory. Journal of Geophysical Research, 91(C6): 7743–7752, doi: 10.1029/JC091iC06p07743

Toporkov J V, Brown G S. 2000. Numerical simulations of scattering from time-varying, randomly rough surfaces. IEEE Transactions on Geoscience and Remote Sensing, 38(4): 1616–1625, doi: 10.1109/36.851961

Verspeek J, Stoffelen A, Verhoef A, et al. 2012. Improved ASCAT wind retrieval using NWP ocean calibration. IEEE Transactions on Geoscience and Remote Sensing, 50(7): 2488–2494, doi: 10.1109/TGRS.2011.2180730

Wang Yunhua, Zhang Yanmin. 2011. Investigation on Doppler shift and bandwidth of backscattered echoes from a composite sea surface. IEEE Transactions on Geoscience and Remote Sensing, 49(3): 1071–1081, doi: 10.1109/TGRS.2010.2070071

Wang Yunhua, Zhang Yanmin, Guo Lixin. 2013. Microwave Doppler spectra of sea echoes at high incidence angles: influences of large-scale waves. Progress in Electromagnetics Research B, 48: 99–113, doi: 10.2528/PIERB12123004

Wang Yunhua, Zhang Yanmin, He Mingxia, et al. 2012. Doppler spectra of microwave scattering fields from nonlinear oceanic surface at moderate- and low-grazing angles. IEEE Transactions on Geoscience and Remote Sensing, 50(4): 1104–1116, doi: 10.1109/TGRS.2011.2164926

Wang Yunhua, Zhang Yanmin, Li Huimin, et al. 2016. Doppler spectrum of microwave SAR signals from two-dimensional time-varying sea surface. Journal of Electromagnetic Waves and Applications, 30(10): 1265–1276, doi: 10.1080/09205071.2016.1186575

Wright J W, Keller W C. 1971. Doppler spectra in microwave scattering from wind waves. The Physics of Fluids, 14(3): 466–474, doi: 10.1063/1.1693458

Zavorotny V U, Voronovich A G. 1998. Two-scale model and ocean radar Doppler spectra at moderate- and low-grazing angles. IEEE Transactions on Antennas and Propagation, 46(1): 84–92, doi: 10.1109/8.655454

Appendix: the CSAR-DOP model

The formula of the fitting model to calculate the Doppler shift for HH and VV polarizations is given as

$$f_{\mathrm{D}}^{\mathrm{PP}}(\theta,\phi,U_{10}) = C_1^{\mathrm{PP}}(\theta,U_{10})\cos\phi + C_2^{\mathrm{PP}}(\theta,U_{10})\left(1+\cos(2\phi)\right), \tag{A1}$$

$$C_n^{\mathrm{PP}} = \sum_{j=1}^{8}\left[\sum_{i=1}^{8}\zeta_n^{\mathrm{PP}}(i,j)U_{10}^{8-i}\right]\theta^{8-j}.$$

The values of the coefficient $\zeta_n^{PP}(i,j)$ are summarized in Tables A1 and A2.

Table A1. The values of the coefficients $\zeta_n^{\mathrm{HH}}(i,j)$

i	n	j							
		1	2	3	4	5	6	7	8
1	1	$3.289\,842\,412\times10^{-13}$	$-7.613\,424\,939\times10^{-11}$	$7.476\,819\,196\times10^{-9}$	$-4.035\,077\,782\times10^{-7}$	$1.290\,773\,364\times10^{-5}$	$-2.443\,514\,578\times10^{-4}$	$2.529\,835\,628\times10^{-3}$	$-1.103\,463\,853\times10^{-2}$
2		$-1.800\,454\,336\times10^{-11}$	$4.184\,966\,785\times10^{-9}$	$-4.129\,019\,773\times10^{-7}$	$2.239\,210\,813\times10^{-5}$	$-7.199\,064\,348\times10^{-4}$	$1.369\,820\,268\times10^{-2}$	$-1.425\,509\,891\times10^{-1}$	$6.250\,136\,956\times10^{-1}$
3		$3.965\,578\,291\times10^{-10}$	$-9.264\,526\,013\times10^{-8}$	$9.190\,097\,791\times10^{-6}$	$-5.012\,182\,761\times10^{-4}$	$1.620\,911\,366\times10^{-2}$	$-3.102\,860\,074\times10^{-1}$	$3.248\,778\,882$	$-1.433\,421\,070\times10^{1}$
4		$-4.506\,209\,974\times10^{-9}$	$1.058\,900\,208\times10^{-6}$	$-1.056\,906\,381\times10^{-4}$	$5.801\,854\,260\times10^{-3}$	$-1.889\,029\,796\times10^{-1}$	$3.641\,439\,530$	$-3.840\,046\,829\times10^{1}$	$1.707\,156\,727\times10^{2}$
5		$2.819\,302\,974\times10^{-8}$	$-6.668\,504\,091\times10^{-6}$	$6.702\,307\,530\times10^{-4}$	$-3.706\,121\,060\times10^{-2}$	$1.215\,862\,353$	$-2.362\,218\,077\times10^{1}$	$2.511\,272\,828\times10^{2}$	$-1.126\,321\,622\times10^{3}$
6		$-9.629\,554\,840\times10^{-8}$	$2.293\,954\,028\times10^{-5}$	$-2.322\,899\,185\times10^{-3}$	$1.294\,510\,077\times10^{-1}$	$-4.281\,071\,498$	$8.385\,954\,444\times10^{1}$	$-8.990\,702\,426\times10^{2}$	$4.071\,242\,902\times10^{3}$
7		$1.655\,738\,416\times10^{-7}$	$-3.973\,796\,527\times10^{-5}$	$4.055\,290\,353\times10^{-3}$	$-2.278\,077\,143\times10^{-1}$	$7.595\,477\,890$	$-1.500\,170\,510\times10^{2}$	$1.621\,963\,723\times10^{3}$	$-7.414\,893\,546\times10^{3}$
8		$-1.108\,360\,248\times10^{-7}$	$2.679\,710\,310\times10^{-5}$	$-2.755\,464\,698\times10^{-3}$	$1.559\,878\,218\times10^{-1}$	$-5.241\,433\,868$	$1.043\,286\,591\times10^{2}$	$-1.136\,699\,362\times10^{3}$	$5.243\,532\,490\times10^{3}$
1	2	$4.773\,190\,435\times10^{-14}$	$-1.231\,589\,865\times10^{-11}$	$1.329\,745\,962\times10^{-9}$	$-7.798\,718\,568\times10^{-8}$	$2.685\,661\,886\times10^{-6}$	$-5.433\,738\,259\times10^{-5}$	$5.981\,800\,220\times10^{-4}$	$-2.764\,438\,049\times10^{-3}$
2		$-2.521\,780\,202\times10^{-12}$	$6.575\,962\,454\times10^{-10}$	$-7.167\,148\,543\times10^{-8}$	$4.239\,848\,419\times10^{-6}$	$-1.471\,970\,274\times10^{-4}$	$3.001\,202\,819\times10^{-3}$	$-3.328\,331\,356\times10^{-2}$	$1.549\,048\,319\times10^{-1}$
3		$5.261\,685\,854\times10^{-11}$	$-1.391\,895\,566\times10^{-8}$	$1.535\,970\,723\times10^{-6}$	$-9.187\,977\,791\times10^{-5}$	$3.222\,688\,631\times10^{-3}$	$-6.634\,073\,212\times10^{-2}$	$7.424\,082\,378\times10^{-1}$	$-3.485\,168\,506$
4		$-5.526\,685\,222\times10^{-10}$	$1.491\,578\,765\times10^{-7}$	$-1.673\,727\,655\times10^{-5}$	$1.015\,873\,724\times10^{-3}$	$-3.609\,993\,783\times10^{-2}$	$7.520\,794\,328\times10^{-1}$	$-8.510\,474\,272$	$4.037\,348\,353\times10^{1}$
5		$3.105\,735\,447\times10^{-9}$	$-8.624\,392\,087\times10^{-7}$	$9.899\,805\,561\times10^{-5}$	$-6.123\,834\,011\times10^{-3}$	$2.212\,244\,344\times10^{-1}$	$-4.676\,787\,040$	$5.363\,065\,611\times10^{1}$	$-2.576\,043\,198\times10^{2}$
6		$-9.329\,340\,404\times10^{-9}$	$2.693\,365\,950\times10^{-6}$	$-3.183\,176\,197\times10^{-4}$	$2.015\,330\,673\times10^{-2}$	$-7.422\,279\,953\times10^{-1}$	$1.595\,267\,787\times10^{1}$	$-1.856\,180\,808\times10^{2}$	$9.035\,885\,003\times10^{2}$
7		$1.429\,688\,153\times10^{-8}$	$-4.310\,355\,133\times10^{-6}$	$5.251\,695\,974\times10^{-4}$	$-3.402\,657\,230\times10^{-2}$	$1.276\,544\,909$	$-2.786\,157\,002\times10^{1}$	$3.284\,966\,881\times10^{2}$	$-1.618\,378\,670\times10^{3}$
8		$-8.812\,708\,015\times10^{-9}$	$2.766\,429\,979\times10^{-6}$	$-3.461\,461\,734\times10^{-4}$	$2.286\,561\,504\times10^{-2}$	$-8.708\,221\,129\times10^{-1}$	$1.924\,040\,411\times10^{1}$	$-2.292\,171\,643\times10^{2}$	$1.139\,834\,252\times10^{3}$

Table A2. The values of the coefficients $\zeta_n^{\mathrm{VV}}(i,j)$

i	n	j							
		1	2	3	4	5	6	7	8
1	1	$4.175\,199\,762\times10^{-13}$	$-9.779\,637\,348\times10^{-11}$	$9.711\,071\,135\times10^{-9}$	$-5.292\,187\,408\times10^{-7}$	$1.706\,771\,784\times10^{-5}$	$-3.251\,799\,715\times10^{-4}$	$3.382\,419\,820\times10^{-3}$	$-1.479\,496\,530\times10^{-2}$
2		$-2.338\,269\,420\times10^{-11}$	$5.502\,331\,045\times10^{-9}$	$-5.489\,265\,151\times10^{-7}$	$3.005\,430\,168\times10^{-5}$	$-9.737\,792\,363\times10^{-4}$	$1.863\,818\,804\times10^{-2}$	$-1.947\,507\,311\times10^{-1}$	$8.557\,272\,135\times10^{-1}$
3		$5.276\,869\,037\times10^{-10}$	$-1.248\,176\,586\times10^{-7}$	$1.251\,737\,029\times10^{-5}$	$-6.889\,478\,573\times10^{-4}$	$2.244\,018\,331\times10^{-2}$	$-4.317\,777\,782\times10^{-1}$	$4.535\,601\,507$	$-2.003\,735\,235\times10^{1}$
4		$-6.146\,295\,843\times10^{-9}$	$1.462\,187\,533\times10^{-6}$	$-1.474\,887\,096\times10^{-4}$	$8.165\,345\,078\times10^{-3}$	$-2.675\,364\,473\times10^{-1}$	$5.178\,688\,042$	$-5.473\,292\,395\times10^{1}$	$2.433\,545\,504\times10^{2}$
5		$3.939\,606\,599\times10^{-8}$	$-9.431\,004\,800\times10^{-6}$	$9.573\,232\,066\times10^{-4}$	$-5.333\,955\,100\times10^{-2}$	$1.759\,025\,809$	$-3.427\,532\,919\times10^{1}$	$3.647\,351\,533\times10^{2}$	$-1.633\,746\,063\times10^{3}$
6		$-1.377\,198\,406\times10^{-7}$	$3.318\,786\,996\times10^{-5}$	$-3.391\,309\,087\times10^{-3}$	$1.902\,198\,967\times10^{-1}$	$-6.315\,337\,528$	$1.238\,982\,626\times10^{2}$	$-1.327\,759\,834\times10^{3}$	$5.994\,733\,167\times10^{3}$
7		$2.423\,949\,707\times10^{-7}$	$-5.881\,020\,705\times10^{-5}$	$6.050\,139\,991\times10^{-3}$	$-3.416\,312\,445\times10^{-1}$	$1.141\,799\,461\times10^{1}$	$-2.255\,069\,936\times10^{2}$	$2.433\,268\,227\times10^{3}$	$-1.107\,079\,110\times10^{4}$
8		$-1.660\,428\,056\times10^{-7}$	$4.054\,823\,598\times10^{-5}$	$-4.198\,095\,695\times10^{-3}$	$2.385\,381\,078\times10^{-1}$	$-8.021\,540\,455$	$1.593\,924\,990\times10^{2}$	$-1.730\,363\,834\times10^{3}$	$7.928\,341\,941\times10^{3}$
1	2	$8.219\,619\,103\times10^{-14}$	$-2.039\,228\,127\times10^{-11}$	$2.132\,100\,659\times10^{-9}$	$-1.217\,674\,249\times10^{-7}$	$4.101\,741\,548\times10^{-6}$	$-8.146\,552\,560\times10^{-5}$	$8.828\,697\,250\times10^{-4}$	$-4.025\,254\,758\times10^{-3}$
2		$-4.421\,519\,680\times10^{-12}$	$1.105\,262\,694\times10^{-9}$	$-1.164\,041\,329\times10^{-7}$	$6.695\,302\,271\times10^{-6}$	$-2.271\,016\,557\times10^{-4}$	$4.541\,214\,326\times10^{-3}$	$-4.954\,005\,434\times10^{-2}$	$2.273\,074\,924\times10^{-1}$
3		$-2.088\,422\,809\times10^{-8}$	$5.743\,443\,516\times10^{-6}$	$-6.569\,015\,358\times10^{-4}$	$-1.470\,151\,475\times10^{-4}$	$5.029\,421\,432\times10^{-3}$	$-1.014\,023\,623\times10^{-1}$	$1.115\,006\,373$	$-5.155\,165\,044$
4		$3.229\,476\,939\times10^{-8}$	$-8.712\,338\,851\times10^{-6}$	$9.811\,908\,000\times10^{-4}$	$1.652\,811\,648\times10^{-3}$	$-5.712\,999\,749\times10^{-2}$	$1.163\,216\,132$	$-1.291\,088\,622\times10^{1}$	$6.023\,001\,716\times10^{1}$
5		$-1.963\,109\,414\times10^{-8}$	$5.193\,633\,421\times10^{-6}$	$-5.755\,104\,939\times10^{-4}$	$-1.020\,219\,335\times10^{-2}$	$3.568\,540\,507\times10^{-1}$	$-7.346\,794\,449$	$8.239\,899\,703\times10^{1}$	$-3.882\,414\,311\times10^{2}$
6		$6.058\,391\,673\times10^{-9}$	$-1.573\,789\,770\times10^{-6}$	$1.716\,755\,002\times10^{-4}$	$3.467\,621\,301\times10^{-2}$	$-1.227\,986\,358$	$2.556\,705\,751\times10^{1}$	$-2.897\,425\,015\times10^{2}$	$1.378\,716\,557\times10^{3}$
7		$-1.024\,581\,334\times10^{-9}$	$2.619\,537\,342\times10^{-7}$	$-2.817\,276\,430\times10^{-5}$	$-5.994\,241\,803\times10^{-2}$	$2.148\,477\,481$	$-4.521\,399\,367\times10^{1}$	$5.173\,981\,343\times10^{2}$	$-2.484\,547\,106\times10^{3}$
8		$9.441\,284\,905\times10^{-11}$	$-2.383\,348\,883\times10^{-8}$	$2.533\,458\,892\times10^{-6}$	$4.064\,923\,949\times10^{-2}$	$-1.472\,987\,336$	$3.129\,561\,803\times10^{1}$	$-3.611\,845\,084\times10^{2}$	$1.748\,083\,996\times10^{3}$